



Kent Academic Repository

Qi, Qi, Hossain, Md. Moinul, Lei, Gang, Wang, Tianxiang, Ling, Tianxiang and Xu, Chuanlong (2022) *Optimum angular arrangement of a multi-light field imaging technique for flame temperature reconstruction*. *Measurement*, 204 . ISSN 0263-2241.

Downloaded from

<https://kar.kent.ac.uk/97688/> The University of Kent's Academic Repository KAR

The version of record is available from

<https://doi.org/10.1016/j.measurement.2022.112110>

This document version

Author's Accepted Manuscript

DOI for this version

Licence for this version

CC BY-NC-ND (Attribution-NonCommercial-NoDerivatives)

Additional information

Versions of research works

Versions of Record

If this version is the version of record, it is the same as the published version available on the publisher's web site. Cite as the published version.

Author Accepted Manuscripts

If this document is identified as the Author Accepted Manuscript it is the version after peer review but before type setting, copy editing or publisher branding. Cite as Surname, Initial. (Year) 'Title of article'. To be published in *Title of Journal*, Volume and issue numbers [peer-reviewed accepted version]. Available at: DOI or URL (Accessed: date).

Enquiries

If you have questions about this document contact ResearchSupport@kent.ac.uk. Please include the URL of the record in KAR. If you believe that your, or a third party's rights have been compromised through this document please see our [Take Down policy](https://www.kent.ac.uk/guides/kar-the-kent-academic-repository#policies) (available from <https://www.kent.ac.uk/guides/kar-the-kent-academic-repository#policies>).

Optimum angular arrangement of a multi-light field imaging technique for flame temperature reconstruction

Abstract

A burner array produces a multi-modal flame temperature field and a compact combustion region. A multi-light field imaging technique can retrieve the multi-modal flame temperature accurately. However, the angular arrangement of the multi-light field imaging technique is a crucial factor that affects the accuracy of the temperature reconstruction. In this study, a method is proposed by integrating a Quantum-behaved Particle Swarm Optimization algorithm to optimise the angular arrangement of the multi-light field imaging technique and to achieve optimal accuracy of the flame temperature reconstruction. The proposed method is evaluated through numerical and experimental studies. The proposed method is also evaluated under different angular arrangements of the multi-light field camera system. Numerical results demonstrate that the optimal angular arrangement provides better reconstruction accuracy in comparison with different angular arrangements. The experimental results of the reconstructed temperature distributions of ethylene-air bimodal diffusion flames show that the proposed method has good applicability.

Keywords

Light field camera, Temperature measurement, QPSO, Angular arrangement, Optimization

1. Introduction

A burner array is widely used in gas-turbine to improve the combustion efficiency which provides a distributed combustion with a compact region [1]. The burner array produces various flames and the temperature field [2-4]. However, for an in-depth understanding of burner array flames, various measurement techniques have been developed [5, 6]. Compared with the intrusive technique, non-intrusive techniques have been used widely owing to don't interfering with the flame flow field and combustion processes, such as acoustic [7], laser-based [8, 9], and radiative imaging [10, 11] techniques. However, the instruments used for the laser-based techniques are complicated thus they are unsuitable for industrial environments. The imaging-based techniques are easy to setup compared to laser-based techniques and use radiative information to measure the flame temperature fields [12, 13]. Whereas the conventional camera records flame projection from a specific angle. Therefore multi-camera (normally 4 [14] to 48 [15] cameras are necessary) system is needed to record multiple projections from the entire array of flames and also to operate all cameras simultaneously. However, the sampling angles of tracing rays of the conventional camera are large and thus provide poor sampling accuracy and affect reconstruction accuracy [16].

Recently, the light field camera (LFC) has attracted significant attention to resolve the aforementioned problems. The direction of sampling rays is more accurate than the conventional camera [17, 18] as the ray's sampling angle of the LFC is much smaller. The more accurate the direction of the ray, the more conducive to the flame temperature reconstruction [19]. A single LFC system or combined with other techniques (such as the background-oriented schlieren technique) was used to retrieve the 2-D or 3-D flame temperature [16, 20]. A LFC along with a linearly variable wavelength was developed to measure the 2-D flame temperature instantaneously [21]. Kim H M et al. [22, 23] adopted the varifocal length and wide field of view lenses to increase the sampling capacity of the LFC. The depth of field and field of view extended up to $\sim 15\text{m}$ and 60° , respectively. Moreover, some studies have been made to investigate the sampling characteristics of the LFC. Such as, Liu et al. [24] investigated the LFC sampling characteristics and stated that the single LFC could only provide limited angular information. For example, For the Lytro Illum LFC, about 200 pixels are covered per microlens. However, under each microlens, the angles corresponding to detected rays are between 21.5° to 23.5° , thus the sampling information provided by adjacent rays is similar. The flame produced by the burner array is multi-modal, irregular and complex. Although a single LFC provides a simple acquisition system of flame radiation, the information collected by the single LFC is limited and insufficient to resolve a complex field.

The multi-LFC system increases the directional diversity and has been utilized to obtain more sampling information. Such as, Liu et al. [24] discussed the multiple LF imaging under the context of flame/flow and suggested that an additional LFC could increase the robustness and temperature/velocity reconstruction accuracy. Two LFCs with an orthogonal arrangement and the Landweber iteration algorithm were utilized to retrieve the 2-D temperature distribution [25]. A multi-plenoptic camera with an orthogonal arrangement system was also developed for the 3-D irregular and multi-modal flame

temperature measurement [26]. Niu et al. [27] applied two LFCs to obtain radiative intensity from two fixed directions for reconstructing the axisymmetric and non-axisymmetric flame temperature, absorption and scattering coefficient distributions. La Foy et al. [28] used two LFCs to improve the reconstruction fidelity and angular resolution of the 3-D fluid velocity field. Even though numerous studies have been done on the multi-LFC system, in most studies, the camera system is either orthogonal layout or arranged at equal angles along the circumference.

The angular arrangement on reconstruction quality has also been investigated, as the angular arrangement of the multi-LFC system influences the reconstruction accuracy. For instance, Fahringer et al. [29] developed a 3-D particle image velocimetry (PIV) from multiple plenoptic cameras to improve the reconstruction quality of the velocity of the ring vortex. The angular separation on the reconstruction quality was discussed and found that the maximum quality was obtained at approximately 75° . Mei et al. [30] used a dual LFC system to reduce the elongation effects of the reconstructed particles and improve the depth resolution in the PIV. The angle separation between two LFCs was investigated and found that the reconstruction quality varied with the angular separation and the optimal reconstruction quality was reached at an angular separation of 90° . However, these studies focused on the comparison of the reconstruction quality at different angular separations for the dual-LFC system, whereas did not provide specific angular arrangement information. Moreover, for the multi-LFC system, there is also a lack of research on the angular arrangement optimization method. As the burner arrays produce different flame structures, thus a targeted optimization of the camera's angular arrangement for different flames under the different multi-LFC systems are crucial to improve the reconstruction fidelity.

Therefore, it is necessary to develop an angular arrangement optimization method for the multi-LF imaging technique. The essence of the optimised angular arrangement method is a multi-objective optimization problem. To solve that, Heuristic algorithms are widely used due to their strong robustness and simpleness [31, 32]. The Quantum-behaved Particle Swarm Optimization (QPSO) algorithm inspired by the principle of traditional particle swarm algorithm and quantum physics is also used. It overcomes the shortcomings of the standard particle swarm optimization algorithm, such as slow convergence speed and eases to fall into local extremums [9]. The QPSO algorithm successfully solved the multi-objective optimization of composite components [33], the inverse radiation and phase change problems [34], and the optimization of the codon usage of the synthetic gene [35], etc.

In this study, a novel method is proposed to optimise the angular arrangement of the multi-LFC system for achieving optimal reconstruction accuracy. In this method, the condition number of the coefficient matrix of the reconstruction equation is selected as the objective function. The QPSO algorithm is used to optimise the angular arrangement of the multi-LFC system. The proposed method is evaluated through systematic simulations under various angular arrangements, flame temperature distributions, and multi-LFC systems. Experiments were conducted on ethylene-air bimodal diffusion flames to reconstruct the temperature and thus verify the applicability of the proposed method. The simulation and experimental results are analysed and discussed.

2. Multi-light field imaging technique

The multi-LF imaging technique consists of a multi-LFC system, LF imaging model and flame radiative transfer model. Fig. 1 exhibits the working principle of the multi-LF imaging technique, which comprises the following steps. Step 1: Image acquisition: Multiple LFCs are synchronized and controlled simultaneously to capture LF flame images under different angular arrangements as described in Section 2.1. Step 2: Ray tracing: To obtain the LF spatial and angular information accurately, the LF imaging model is used to trace the rays from the photosensor to the flame as described in Section 2.2. The final step is to combine the information from the multi-LFC system to reconstruct 3-D flame temperature distributions through a reconstruction algorithm as described in Sections 2.3 and 4.1.

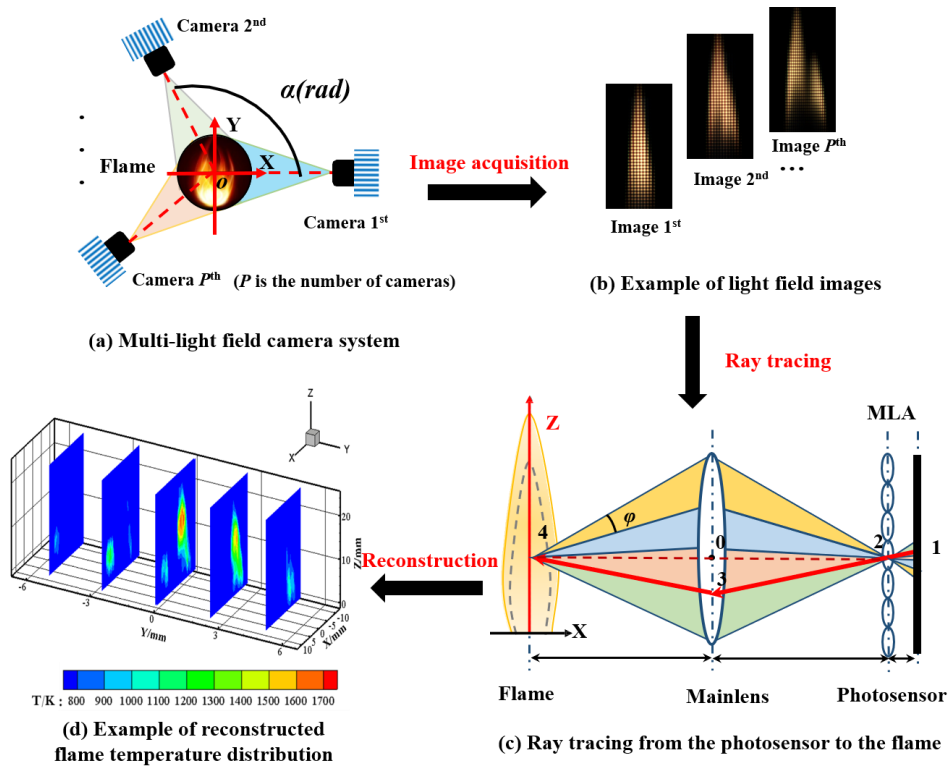


Fig. 1 Working principle of a multi-LF imaging technique for flame temperature reconstruction.

To facilitate the flame temperature reconstruction from a multi-LFC system, a common world coordinate is used and defined in Fig. 1. Where the Z-axis is perpendicular to the flame cross-section, the X-axis is the opposite direction of the photosensor normal vector and the Y-axis is the horizontal direction. Regardless of the number of LFCs or their angles of separation, the world coordinate system (X, Y, Z) does not change.

2.1 Multi-LFC arrangement

Multi-LFC system consists of multiple identical LFCs. The camera's arrangement is mainly co-planar. The cameras are arranged at different angles around the Z flame as shown in Fig. 1 (a). The multiple cameras are synchronized by camera software to capture flame images from different perspectives, simultaneously. The procedures of cameras calibrated with each other can be found in Ref. [26]. The multi-modal structure of the flame can be captured from different angles, however, at some angles, the

multi-modal structure can not be captured due to the flame modals overlapping at this viewing angle. These different multi-modal images provide diverse LF information. To obtain adequate LF radiative information and to achieve better reconstruction accuracy, it is necessary to place cameras at optimum angular arrangements. The proposed angular arrangement optimization method of the multi-LFC system is described in Section 3.

2.2 LF imaging model

In the multi-LFC system, each camera is treated quasi-independently. As a result, the imaging model of the single LFC is the basis of the multi-LFC system. Compared with the conventional camera, the sampling angle φ of the LFC is much smaller, so the direction of a sampling ray is more accurate [16]. This allows the LFC to simultaneously obtain spatial and angular information in a single exposure through the following equations:

$$\frac{1}{s_v} + \frac{1}{s} = \frac{1}{F} \quad (1)$$

$$\frac{x_v}{x_m} = -\frac{s_v}{s} \quad (2)$$

where s_v and s denote the object and image distance of the lens, respectively; x_v and x_m are the coordinates of the object point and image point, respectively; F is the focal length of the lens; For the main lens, s_v is equal to the distance between the main lens and object plane, s represents the distance between the main lens and the microlens array (MLA), x_v is the coordinate of point 4 (x_4, y_4, z_4); x_m is the coordinate of point 2 (x_2, y_2, z_2), F is the focal length of the main lens; For the microlens, s is the distance between the main lens and MLA; s is equal to the distance between MLA and CCD; x_v is the coordinate of point 3 (x_3, y_3, z_3); x_m is the coordinate of point 1 (x_1, y_1, z_1), and F is the focal length of the microlens. Therefore, the coordinates of the ray passing through the respective planes can be derived according to the Eqs. (1) and (2). The polar angle θ and azimuthal angle Ψ are used to represent the direction of the ray, which can be calculated through the following equations:

$$\theta = \arccos \left[\frac{(z_3 - z_4)}{\sqrt{(y_3 - y_4)^2 + (z_3 - z_4)^2 + s_v^2}} \right] \quad (3)$$

$$\psi = \begin{cases} \arctan \left(\frac{y_3 - y_4}{x_3 - x_4} \right), y_3 \geq y_4 \\ \arctan \left(\frac{y_3 - y_4}{x_3 - x_4} \right) + 2\pi, y_3 < y_4 \end{cases} \quad (4)$$

2.3 Flame radiative transfer model

After obtaining the spatial and direction of the ray, the next step is to establish the relationship between the outgoing radiative intensity at the boundary surface and the internal radiation of a flame. It is the basis for realizing the 3-D flame temperature distribution reconstruction. The outgoing radiative intensity at the boundary surface of a flame is the accumulation of radiative intensity of all object points

along the propagation path. The radiative transfer process within the flame can be described by the Radiative Transfer Equation (RTE) [36]. Due to soot being absorptive particles, the scattering effect of the soot particles can be ignored during radiative intensity calculation [37]. If the propagation path discrete into n parts and each part maintains an approximately uniform temperature, the radiative intensity at the flame boundary in the Ω direction can be calculated through the discretized RTE as follows:

$$I_{\lambda}(\Omega) = I_{b\lambda}^n [1 - \exp(-\tau_{\lambda n})] + \sum_{i=1}^{n-1} \left[\exp\left(-\sum_{j=i+1}^n \tau_{\lambda j}\right) - \exp\left(-\sum_{j=i}^n \tau_{\lambda j}\right) \right] I_{b\lambda}^i \quad (5)$$

where τ_{λ} denotes the optical thickness; I_{λ} represents the spectral radiative intensity of the ray passing through the flame; $I_{b\lambda}$ is the spectral blackbody radiative intensity. By integrating the RTE in various directions, the outgoing flame radiative intensity recorded by the photosensor can be obtained. It can be represented in the form of a matrix and expressed as follows:

$$\begin{bmatrix} I_{\lambda}^1 \\ I_{\lambda}^2 \\ \mathbf{M} \\ I_{\lambda}^M \end{bmatrix} = \begin{bmatrix} A_1^1 & A_2^1 & \mathbf{L} & A_N^1 \\ A_1^2 & A_2^2 & \mathbf{L} & A_N^2 \\ \mathbf{M} & \mathbf{M} & \mathbf{O} & \mathbf{M} \\ A_1^M & A_2^M & \mathbf{L} & A_N^M \end{bmatrix} \begin{bmatrix} I_{b\lambda}^1 \\ I_{b\lambda}^2 \\ \mathbf{M} \\ I_{b\lambda}^N \end{bmatrix} \quad (6)$$

where M represents the total number of detection rays, and N is the number of dividing voxels.

In the multi-LFC system, each of the cameras constructs a matrix format equation like Eq. (6). If the number of cameras P are considered in the multi-LFC system, the RTE equation of the multi-light field camera system can be expressed as:

$$\begin{bmatrix} I_{\lambda}^1 \\ I_{\lambda}^2 \\ \mathbf{M} \\ I_{\lambda}^{M \times P} \end{bmatrix} = \begin{bmatrix} A_1^1 & A_2^1 & \mathbf{L} & A_N^1 \\ A_1^2 & A_2^2 & \mathbf{L} & A_N^2 \\ \mathbf{M} & \mathbf{M} & \mathbf{O} & \mathbf{M} \\ A_1^{M \times P} & A_2^{M \times P} & \mathbf{L} & A_N^{M \times P} \end{bmatrix} \begin{bmatrix} I_{b\lambda}^1 \\ I_{b\lambda}^2 \\ \mathbf{M} \\ I_{b\lambda}^N \end{bmatrix} \quad (7)$$

$$\mathbf{I}_{\lambda} = \mathbf{A} \mathbf{I}_{b\lambda} \quad (8)$$

where \mathbf{I}_{λ} is the outgoing radiative intensity distribution vector received by the LFCs. \mathbf{A} is the coefficient matrix. Finally, the temperature T can be solved by Eq. (9) [38].

$$I_{b\lambda}(r) = \frac{c_1 \lambda^{-5}}{\pi \left[e^{c_2 / \lambda T(r)} - 1 \right]} \quad (9)$$

where c_1 and c_2 are the first and second radiation constants, which are $3.7418 \times 10^{-16} \text{ W} \cdot \text{m}^2$ and $1.4388 \times 10^{-2} \text{ m} \cdot \text{K}$, respectively.

As shown in Fig. 2, the number of flame voxels passed by each ray is far less than the total dividing

voxels. As a result, matrix A has the characteristics of sparsity and ill-conditioning with numerous zeros. According to Ref. [39], the condition number $\kappa(A)$ of coefficient matrix A is a fairly good quantitative indicator of ill-conditioning in a system of linear equations. Reducing the ill-conditioning of the equations can increase the accuracy of the solution. The definition of $\kappa(A)$ is as follows:

$$\kappa(A) = \|A\| \cdot \|A^{-1}\| \quad (10)$$

The coefficient matrix A would be different for the different angular arrangements of the cameras, and thus the $\kappa(A)$ will also be different. To achieve the best reconstruction results, the cameras need to be setup with optimal angles resulting in the lowest $\kappa(A)$ of coefficient matrix A .

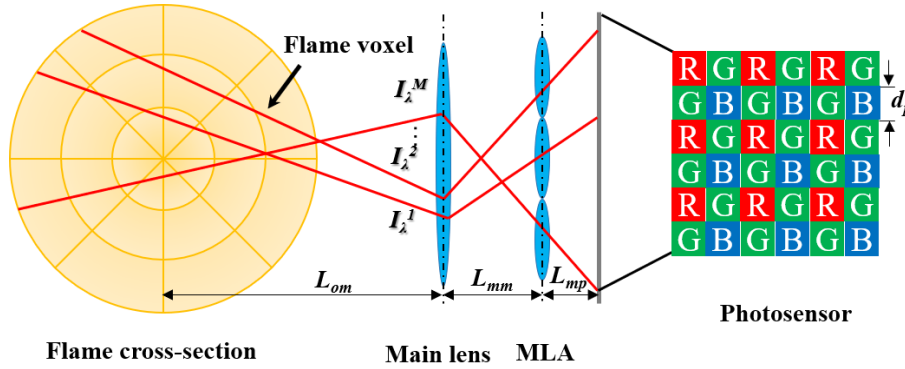


Fig. 2. The schematic diagram of flame radiation sampling with a single LFC.

3. Optimise angular arrangement method

To achieve better reconstruction accuracy, the angular arrangement of the multi-LF imaging technique needs to be optimised. The optimization of the angular arrangement is a multi-objective optimization problem. Heuristic algorithms are widely used to solve multi-objective optimization problems due to their strong robustness and simpleness. As a typical heuristic algorithm, the QPSO algorithm is used in this study. It is a swarm intelligence technique that utilizes group and individual intelligence to solve combinatorial optimization problems. It is also a powerful tool to pinpoint the global minimum under a plethora of local minima and solve multi-objective optimization problems due to its faster convergence speed and difficulty to fall into local extremums [40].

The QPSO algorithm is based on the conceptual model of birds foraging and works as an adaptive and robust parameter searching technique. The flocking population of QPSO is called a swarm and the individuals are called particles. Where, every particle adjusts its position according to the fly experience of itself and its companion, to achieve better self-position and global fitness. For instance, let X be a N_w -dimensional search space and $F_{\text{obj}}(\chi)$ be the objective function defined over X . As the optimization of angular arrangement of the multi-LF imaging technique is a multi-objective optimization problem, so the objective function $F_{\text{obj}}(\chi)$ can be defined as finding a vector, $\chi = (\chi_1, \chi_2, \dots, \chi_{N_w})^T \in X$ that satisfies minimizing $\kappa(A)$ over X . If the swarm contains N_s groups, each group has N_w particles, then each group can be represented as a potential χ . The position of an i th particle can be denoted as $X_i (\forall i = 1, 2, 3, \dots, N_s \times N_w)$ and the position of a k th group can be denoted as $\chi^k = (\chi_{k,1}, \chi_{k,2}, \dots, \chi_{k,N_w}), k \in N_s$. Particles in

each group continuously update themselves through Eqs. (11-13), ultimately converging onto the optimal position.

$$\begin{aligned}
& \text{if } \text{rand}_{u4} > 0.5 \\
& \mathbf{X}_i(t+1) = \mathbf{Q}_i(t) - \beta \times |\mathbf{P}_m(t) - \mathbf{X}_i(t)| \times \ln(1/\text{rand}_{u3}) \\
& \text{else} \\
& \mathbf{X}_i(t+1) = \mathbf{Q}_i(t) + \beta \times |\mathbf{P}_m(t) - \mathbf{X}_i(t)| \times \ln(1/\text{rand}_{u3})
\end{aligned} \tag{11}$$

where,

$$\mathbf{Q}_i(t) = \frac{\text{rand}_{u1} \times \mathbf{P}_i(t) + \text{rand}_{u2} \times \mathbf{P}_g(t)}{\text{rand}_{u1} + \text{rand}_{u2}} \tag{12}$$

$$\mathbf{P}_m(t) = \frac{1}{N_s} \sum_{i=1}^{N_s} \mathbf{P}_i(t) \tag{13}$$

where \mathbf{P}_i is the individual best position defined as the best solution found by the particle during flight; \mathbf{P}_k is the group best position defined as the best solution found by the particles of this group during flight; \mathbf{P}_g is the global best solution which is the best position of the whole flock; rand_{u1} , rand_{u2} , rand_{u3} and rand_{u4} are four uniformly distributed random numbers on $[0, 1]$; β is the contraction-expansion coefficient; $\mathbf{Q}_i(t)$ is the local attractor point; $\mathbf{P}_m(t)$ is the mean best position defined as the mean of all the best positions of the population; The detailed computational procedures of the QPSO algorithm can be found elsewhere in [40, 41].

Fig. 3 provides a detailed implementation procedure of the angular arrangement optimization method of the multi-LF imaging technique. In this study, the condition number $\kappa(\mathbf{A})$ is considered as the objective function F_{obj} in the QPSO algorithm; the particle position \mathbf{X}_i represents the angular arrangement of the camera; the dimension N_w is the number of LFCs; χ represents a kind of arrangement of the multi-LF imaging technique, and the corresponding objective function value that is condition number $\kappa(\mathbf{A})$ is obj_k ; the corresponding objective function value of the multi-LF imaging technique under the optimal arrangement is obj_g .

The procedures for implementing angular arrangement optimization of a multi-LF imaging technique using the QPSO algorithm are described in the following steps:

Step 1. Select input parameters for the variables N_s , N_w , the search space $[\text{low}_j, \text{high}_j]$ ($j=1, 2, \dots, N_w$); the maximum number of iterations N_c .

Step 2. Initialize the position of N_s groups of particles in the N_w -dimensional space randomly. Obtain the initial group and global best position $\mathbf{P}_k(t)$ and $\mathbf{P}_g(t)$, then calculate the corresponding objective function value that is condition number obj_j and obj_g . Set the current iteration number $t=1$.

Step 3. Update the $\mathbf{Q}_i(t)$, $\mathbf{P}_m(t)$, $\mathbf{P}_k(t)$ and $\mathbf{P}_g(t)$ using Eqs.(11-13).

Step 4. Calculate the objective function value that is condition number $F_{\text{obj}}(\chi)$ corresponding to each χ , then compare it with obj_j and obj_g . If $F_{\text{obj}}(\chi) < \text{obj}_j$, update the individual best position \mathbf{P}_i . If

$F_{\text{obj}}(\chi) < \text{obj}_g$, update the global best position P_g .

Step 5. The stop criteria are checked. If the changes of $F_{\text{obj}}(P_g)$ are smaller than the tolerance ε or the iteration number exceeds the maximum iteration number N_c , then proceed to Step 6; otherwise, set $t=t+1$ and return to Step 3.

Step 6. Terminate the program once optimised results are achieved.

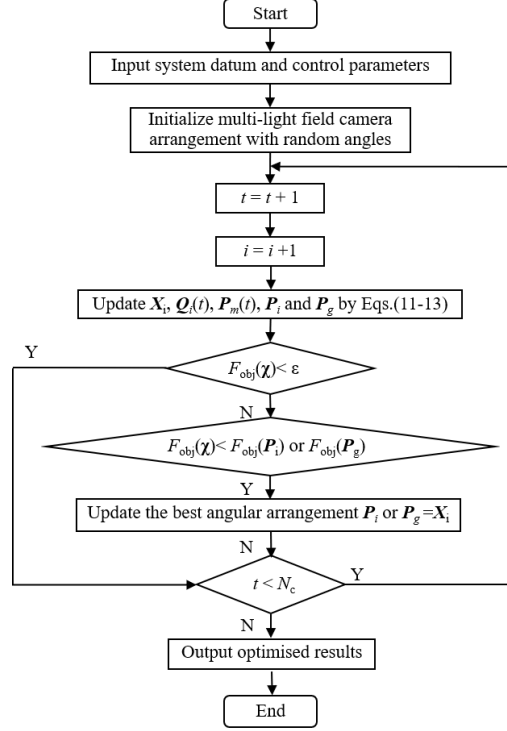


Fig. 3 Implementation procedure of the QPSO algorithm for the optimised angular arrangement of the multi-LF imaging technique.

4. Numerical studies

4.1 Numerical setup

Numerical studies were performed to obtain an optimised angular arrangement for the multi-LF imaging technique. The QPSO algorithm is used as the optimization algorithm and the parameters of the QPSO algorithm are set as: the number of the particles in the swarm is $N_s=20$; the maximum number of iterations is $N_c=2000$; the number of dimensions is $N_w=1, 2, 3$; the search space is $[0^\circ, 360^\circ]$ ($j=1,2,\dots, N_w$); the tolerance of the minimum fitness ε is 10^{-8} . The flame is treated as cylindrical and divided into circumferential(N_ϕ) \times radial(N_r) \times axial(N_z) = $10\times 8\times 6=480$ voxels. The parameters of flame and the LFC used in the numerical studies can be found in Ref. [42]. It is worth noting that, the temperature and absorption coefficient distributions of the burner array's flames are multi-modal and irregular in comparison to a single-nozzle burner. In this study, three different multi-modal distributions such as bimodal, three-modal and four-modal flame temperature and absorption coefficient are considered. In all cases, the temperature range is set from 1000 K to 2000 K, and the absorption coefficient range is considered to be 0-30 m^{-1} [27]. These distributions are generated through the Eqs. (14-15). The

parameters of each multi-modal flame are exhibited in Table 1. The corresponding distributions of flame temperature T and absorption coefficient κ_a are shown in Fig. 4.

$$T(x, y, z) = 600 \sum_{i=1}^n 0.8 \exp \left\{ -40 \left[\frac{(750x+8)}{9} - x_{0,i} \right]^2 - 25 \left[\frac{(750y+8)}{9} - y_{0,i} \right]^2 \right\} + 880(1-100z/3) + 753 \text{ [K]} \quad (14)$$

$$\kappa_a(x, y, z) = \frac{50}{3} \sum_{i=1}^n 0.8 \exp \left\{ -40 \left[\frac{(750x+8)}{9} - x_{0,i} \right]^2 - 25 \left[\frac{(750y+8)}{9} - y_{0,i} \right]^2 \right\} + 20(1-100z/3) + 5/3 \text{ [m}^{-1}\text{]} \quad (15)$$

where n denotes the number of peaks of each flame; $x_{0,i}$ and $y_{0,i}$ are the coordinates of the bottom of the flame modal; x , y , and z are the coordinates of the coordinate system, respectively.

Table 1. The parameters of the multi-modal flames.

| Simulated Flame | Number of modals, n | Coordinate ($x_{0,i}, y_{0,i}$) |
|-----------------|-----------------------|-----------------------------------|
| Bimodal | 2 | (1.20, 090) |
| | | (0.60, 0.90) |
| Three-modal | 3 | (1.20, 1.10) |
| | | (0.60, 1.10) |
| | | (0.90, 0.60) |
| Four-modal | 4 | (1.25, 0.90) |
| | | (0.55, 0.90) |
| | | (0.90, 1.25) |
| | | (0.90, 0.55) |

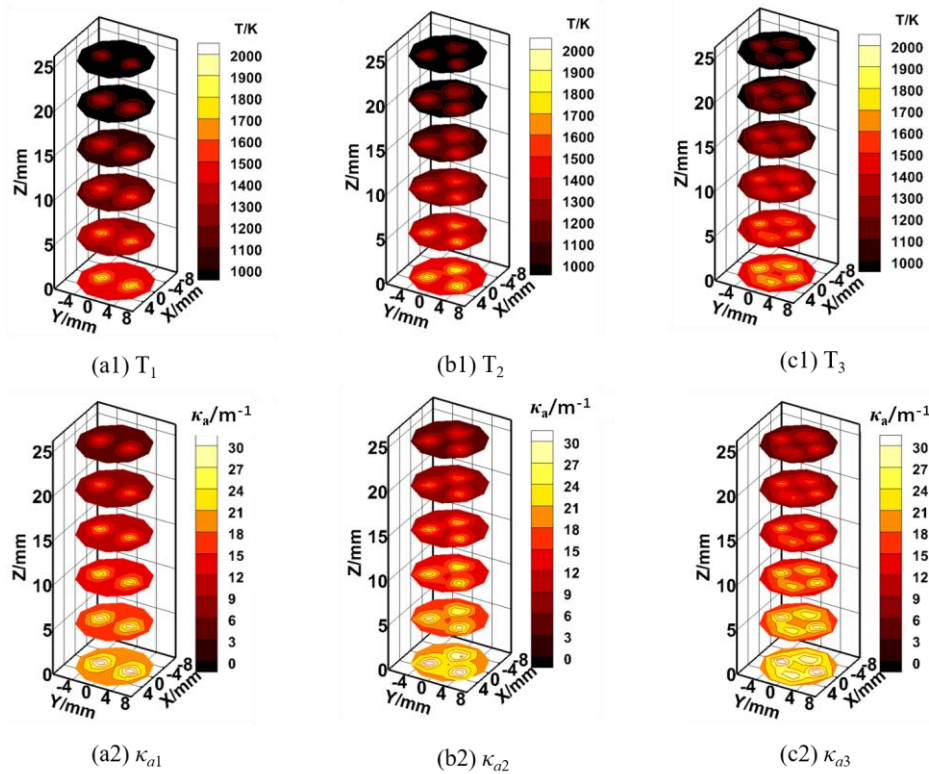


Fig. 4 The bimodal, three-modal and four-modal simulated flame temperature (a1, b1 and c1) and absorption coefficient distributions (a2, b2 and c2).

The Non-Negative Least Squares (NNLS) algorithm is utilized for flame temperature reconstruction

[43]. A detailed description of the NNLS algorithm can be found in Ref. [44]. This algorithm provides non-negative reconstructed results and good stability. Based on the camera specification, the minimum signal-to-noise ratio (SNR) can be set to 60 dB. Therefore, during the reconstruction process, the SNR=55 dB is added to the flame radiative intensity. To evaluate the reconstruction accuracy, the relative error ΔT_i at i th voxel is calculated. The definition of ΔT_i is expressed in Eq. (16). The mean reconstruction relative error ΔT_{mean} is defined as Eq. (17).

$$\Delta T_i = \frac{|T_{rst,i} - T_{ori,i}|}{T_{ori,i}} \quad (16)$$

$$\Delta T_{\text{mean}} = \frac{1}{N} \sum_{i=1}^N \Delta T_i \quad (17)$$

where $T_{rst,i}$ and $T_{ori,i}$ are the reconstructed and original temperatures, respectively.

4.2 Effects of different angular arrangements

To verify the effectiveness of the QPSO algorithm, the optimization process was repeated three times. The angular arrangement of a dual-LFC system for the bimodal flame with temperature (T_1) and absorption coefficient (κ_{a1}) distributions were taken into consideration. Under three repetitions, the corresponding condition numbers $\kappa(\mathcal{A})$ are calculated by Eq. 10 and shown in Fig. 5. The computer used for calculation is Intel(R) Core (TM) i9-9900K CPU @ 3.60GHz. The iteration time of each step is 398s, and the occupied memory is 15665 MB. It can be seen that the initial condition numbers $\kappa(\mathcal{A})$ of each repetition are different due to the initial positions of the particles in the swarm being initialized randomly, i.e., the initial condition numbers $\kappa(\mathcal{A})$ under three repetitions are obtained $3.5088\text{e}+08$, $4.8216\text{e}+09$ and $1.1998\text{e}+10$, respectively. It can be seen that the condition numbers $\kappa(\mathcal{A})$ descend stepwise with the increase of iterations (partially enlarged Fig. 5). Although the initial $\kappa(\mathcal{A})$ of three repetitions are different, the iterations eventually converge to the same condition number $\kappa(\mathcal{A})$, which is $4.0373\text{e}+06$. Thus, it is suggested that the QPSO algorithm is an effective algorithm for optimising the angular arrangement of the multi-LF imaging technique.

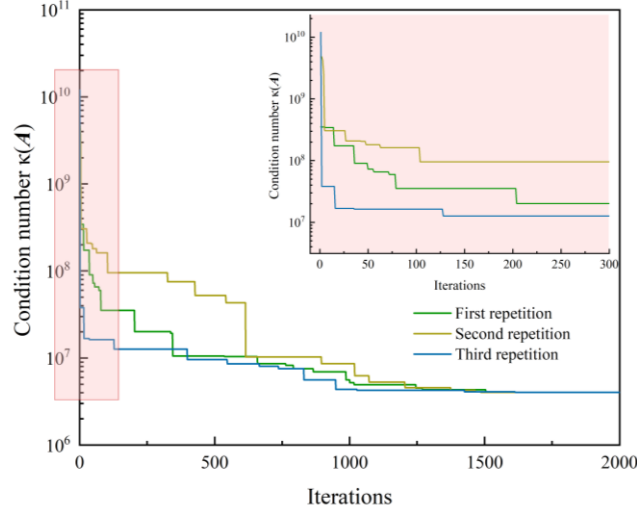


Fig. 5 The objective function values at different iterations.

The final optimal angular arrangement of a dual-LFC system is 174° & 277° under the bimodal flame temperature (T_1) and absorption coefficient (κ_{a1}) distributions. To further verify whether the optimised angular arrangement provides better reconstruction quality for the multi-LFC system, a few typical angular arrangements of the LFCs are considered and the comparative results are shown in Fig. 6. Case 1 is the optimised angular arrangement obtained by the QPSO algorithm; Cases 2 and 3 represent the commonly adopted angular arrangements that distribute the cameras orthogonally [26, 29]; Case 4 is used for comparison which the angular arrangement is developed symmetrically [30]. Numerical simulations were carried out for these four cases. The condition numbers $\kappa(\mathcal{A})$ and temperature reconstruction errors were calculated for each case and shown in Table 2. It can be seen that the condition numbers are varied dramatically from case to case, indicating the angular arrangement of LFCs has a critical effect on the ill-conditioning of the reconstruction. For Case 4, the condition number is very large, which indicates that the ill-conditioning of reconstruction is worse. The maximum reconstruction error reaches 74.90%. Orthogonal arrangements like Cases 2 and 3 also provide poor reconstruction quality. The LF information captured by Case 3 is more conducive to reconstruction than by Case 2, so the condition number $\kappa(\mathcal{A})$ and reconstruction error obtained by Case 3 are smaller. It can be seen that the optimal angular arrangement of the dual-LFC system is obtained for Case 1, when the cameras arrange at the optimal angles, the condition number $\kappa(\mathcal{A})$ is reduced to $4.0373e+06$. Therefore, Case 1 provides a better reconstruction quality than the other cases. It is also suggested that 1) the condition number $\kappa(\mathcal{A})$ is a good quantitative indicator of ill-conditioning of the reconstruction; 2) the optimal angular arrangement of the multi-LF imaging technique optimised by the QPSO algorithm improves the flame temperature reconstruction quality.

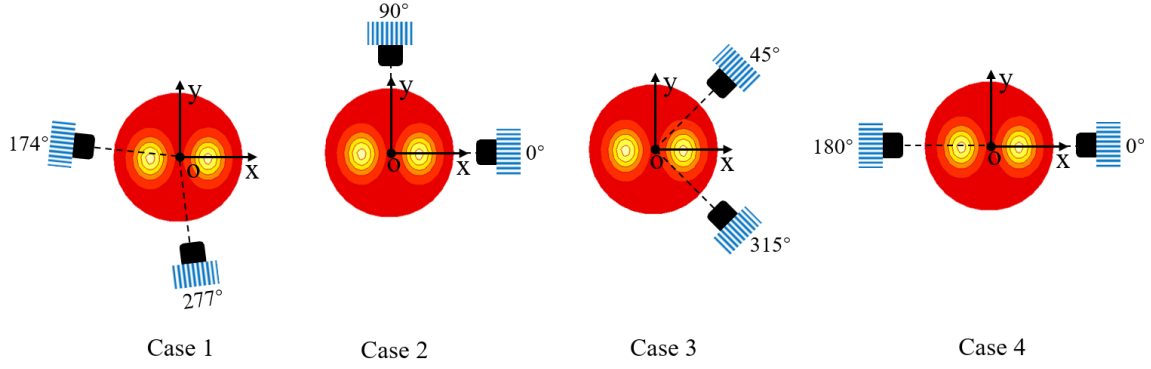


Fig. 6 Angular arrangements of the dual-LFC system.

Table 2. The condition numbers $\kappa(A)$ and temperature reconstruction errors of bimodal flame when two LFCs arrange at various angles.

| Case | Condition Number $\kappa(A)$ | Reconstruction Error | |
|------|------------------------------|----------------------|-------|
| | | Maximum | Mean |
| 1 | 4.0373e+06 | 51.05% | 5.14% |
| 2 | 4.2221e+08 | 59.52% | 6.05% |
| 3 | 3.7710e+07 | 55.19% | 5.65% |
| 4 | 1.0188e+10 | 74.90% | 7.02% |

4.3 Angular arrangement optimization under different multi-LFC systems

It is important to investigate the optimal angular arrangement of the different multi-LFC systems. Because different systems lead to different flame temperature reconstruction accuracy. In this study, the QPSO algorithm is used to optimise the angular arrangement for the bimodal flame temperature (T_1) and absorption coefficient (κ_{a1}) distributions under three multi-LFC systems, which contain single, dual and three-LFCs, respectively. The optimised angular arrangements and the calculated LF images from optimised angles are shown in Table 3 and Fig. 7. It can be seen that different multi-LFC systems occupy different optimal angular arrangements. A camera arranged at 226° is the optimal angular arrangement for the single LFC system, 174° & 277° for the dual-LFC system and 63° & 218° & 316° for the three-LFC system. The simulated LF images from various angles also demonstrated the differences in flame radiative information from different perspectives. As can be seen, when the camera arranges at 277° , two flame modals can be captured explicitly.

The reconstruction performance is investigated for three multi-LFC systems under the bimodal flame. The reconstructed flame temperature and relative error distributions are shown in Fig. 8 and 9. Table 3 also demonstrates the condition numbers $\kappa(A)$, and mean and maximum relative errors of the three systems. It can be seen that among the three systems, the ill-conditioning of reconstruction constructed by the single LFC system is the worst, which the $\kappa(A)=3.0924e+11$. The poorest reconstruction quality

is also achieved, particularly at the top regions of the flame. The three-LFC system demonstrates a higher accuracy than the dual-LFC system. The condition number $\kappa(\mathcal{A})$ and mean relative error for the three-LFC system are only $3.3955e+04$ and 3.20%. The $\kappa(\mathcal{A})$ and reconstruction errors decrease with the increasing number of cameras, indicating that the richer the collected flame radiative information, the more accurate the reconstructed flame temperature. As a consequence, the QPSO algorithm can effectively optimise the angular arrangement of different multi-LFC systems.

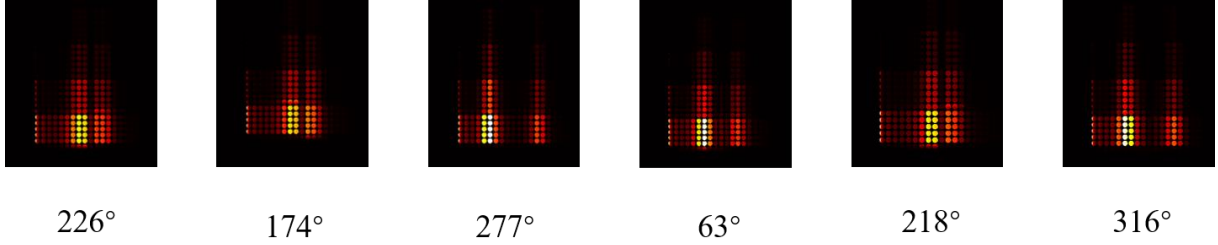


Fig. 7 Example of simulated LF flame images under different angular arrangements.

Table 3. The condition numbers $\kappa(\mathcal{A})$ and temperature reconstruction errors of bimodal flame under different multi-LFC systems.

| Case | Camera System | Arranged angles | Condition number $\kappa(\mathcal{A})$ | Reconstruction error | |
|------|---------------|-----------------|--|----------------------|--------|
| | | | | Maximum | Mean |
| 1 | 1st | 226° | $3.0924e+11$ | 68.83% | 11.16% |
| 2 | 1st | 174° | $4.0373e+06$ | 51.05% | 5.14% |
| | 2nd | 277° | | | |
| 3 | 1st | 63° | $3.3955e+04$ | 41.29% | 3.20% |
| | 2nd | 218° | | | |
| | 3rd | 316° | | | |

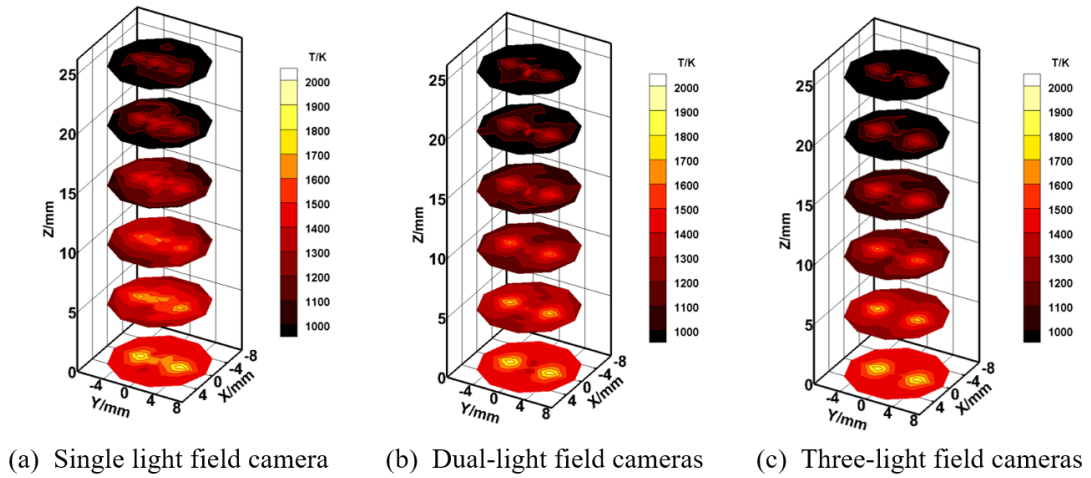
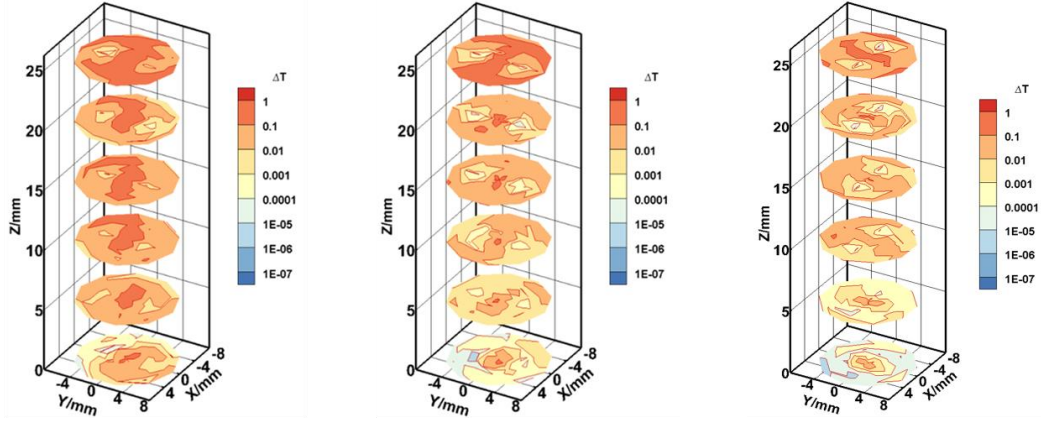


Fig. 8 The reconstructed temperature distributions of bimodal flame under different multi-LFC systems.

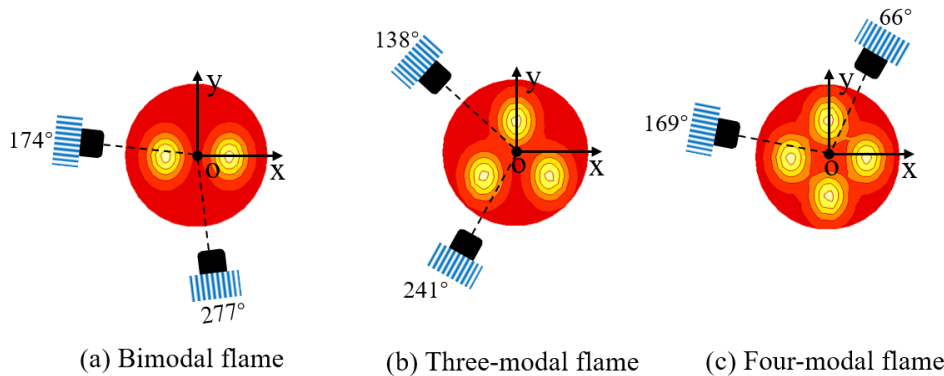


(a) Single light field camera (b) Dual-light field cameras (c) Three-light field cameras

Fig. 9 The relative error distributions of reconstructed bimodal flame temperature under different multi-LFC systems.

4.4 Angular arrangement optimization under different flames

Compared with the single-nozzle burner, the flame temperature and absorption coefficient distributions produced by the burner array are multi-modal and irregular. It is crucial to examine the optimal angular arrangement of the multi-LF imaging technique for different flames. In this study, bimodal, three-modal and four-modal flames are considered. Their corresponding temperature and absorption coefficient distributions are defined by Eqs. (14-15). The QPSO algorithm optimises the angular arrangement of the dual-LFC system under three kinds of flames. Fig. 10 shows the optimal angular arrangements of the dual-LFC system. It can be seen that 174° & 277° , 138° & 241° and 66° & 169° are the optimal angular arrangements for the bimodal, three-modal and four-modal flame, respectively. Even though different flames occupy different optimal arranged angles, the angular separation between two optimised arranged angles of the dual-LFC system is 103° .



(a) Bimodal flame (b) Three-modal flame (c) Four-modal flame

Fig. 10 The optimal arranged angles of the dual-LFC system under different flames.

The flame temperature fields are reconstructed using the radiative information collected by the cameras placed at the optimal angles. The reconstructed flame temperature distributions under three flames are shown in Fig. 11. The corresponding relative errors and condition numbers $\kappa(\mathcal{A})$ are shown in Fig. 12.

It can be seen that there is a small difference between the reconstructed and original temperature. The condition numbers $\kappa(A)$ of the bimodal, three and four-modal flames are $4.0373e+06$, $4.8884e+7$ and $5.3031e+07$, respectively. The reconstruction constructed by the three and four-modal flames has a higher ill-conditioning than the bimodal flame. Due to the weaker ill-conditioning of the bimodal flame, the highest reconstruction quality is obtained. Hence, the QPSO algorithm can optimise the angular arrangement of the multi-LF imaging technique under different flames.

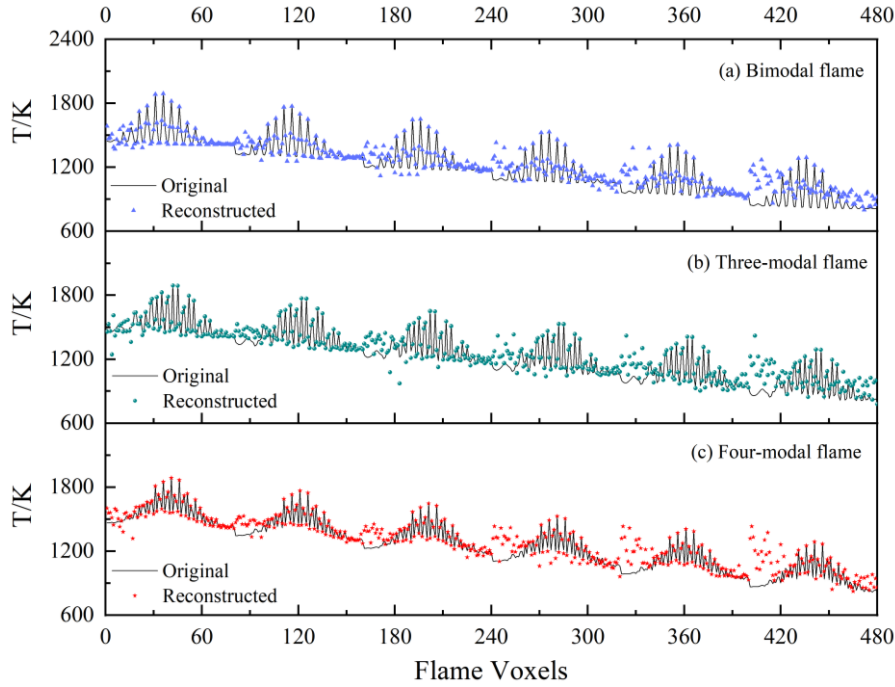


Fig. 11 The reconstructed temperature under different flames and voxels.

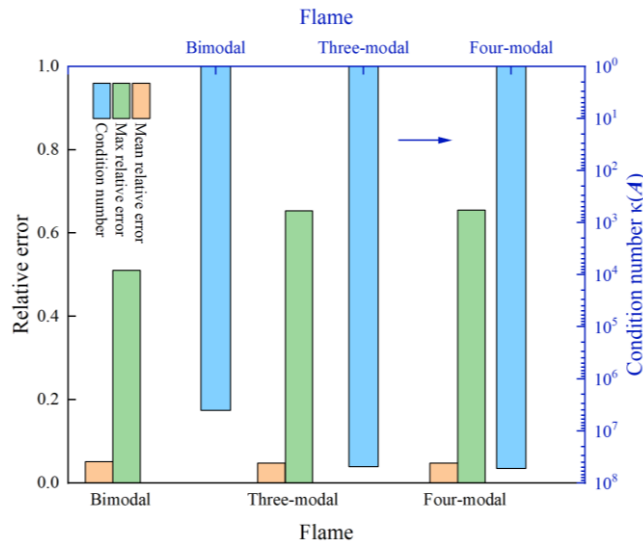


Fig. 12 The condition numbers $\kappa(A)$ and reconstruction errors under different flames.

5. Experimental results and discussions

To evaluate the proposed technique, experiments were conducted on ethylene-air bimodal diffusion flames as shown in Fig. 13. The experimental setup mainly includes a burner and an image acquisition

system which include two LFCs and a computer that is used to capture flame images synchronously. In this study, the cage-type LFC is utilized [26]. The size of the microlens is $100 \times 100 \mu\text{m}$ and $f\# = 4.2$. A Nikon 50mm 1.8D lens is used as the main lens. The CCD sensor of the LFC has a resolution of $3312 \text{ (H)} \times 2488 \text{ (V)}$, and the pixel size is $5.5 \mu\text{m}$. Two LFCs are arranged on a circular slide. Cameras 1st and 2nd are arranged at 174° and 277° , respectively. Both cameras are of the same height and equidistant from the center of the burner. The burner is fixed in the center of a round breadboard. The ethylene fuel is injected through the nozzles on the nozzle plate. The structure of the dual-nozzle plate is shown in Fig. 13. The distance between the centers of the two nozzles is 24 mm. The air is injected through annular nozzles made of glass beads and meshes. The injected air not only provides the oxidizer but also protects the flame from surrounding disturbance [45]. The experiments were carried out in a dark room to avoid stray radiation. Both cameras have the same exposure time of $110 \mu\text{s}$. Three different operation conditions were performed, which are shown in Table 4.

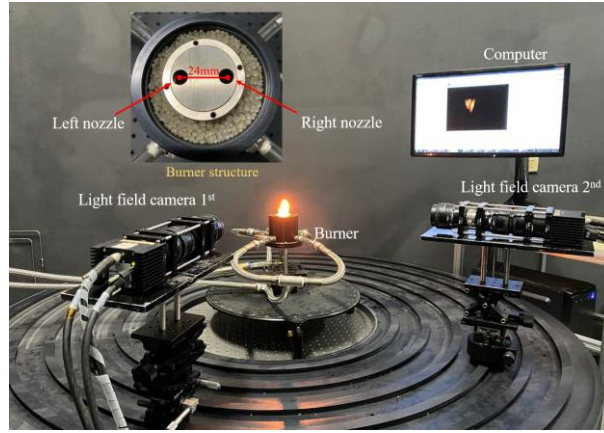


Fig. 13 Experimental setup of a multi-LFC system for bimodal flame temperature reconstruction.

Table 4. Ethylene-air diffusion flame conditions.

| Condition | Ethylene (L/min) | Air (L/min) |
|-----------|------------------|-------------|
| 1 | 0.20 | |
| 2 | 0.25 | 10.00 |
| 3 | 0.30 | |

Fig. 14 shows the captured LF images of bimodal flame under different conditions. It can be seen that the arranged angles of the cameras determine the difference in the captured flame images. Due to the bimodal flame produced by two nozzles being separate, the images captured from Camera 2nd exhibit the two-modal profile of flame. The LF flame images captured by cameras are used to reconstruct the bimodal flame temperature distributions. Before capturing flame, a dark image was collected first to eliminate the noise of the photosensor. The flame was divided into $N_\phi \times N_r \times N_z = 82 \times 80 \times 8 = 52480$ voxels. The flame temperature distribution was reconstructed by the NNLS algorithm. The reconstructed bimodal flame temperature distributions are exhibited in Fig. 15. The highest temperature region appears in the middle of the flame due to the full mixing of fuel and air and the bulk chemical energy released

in this zone. Away from this zone, the temperature gradually decreases, therefore the temperatures between the two peaks and the top of the flame are low.

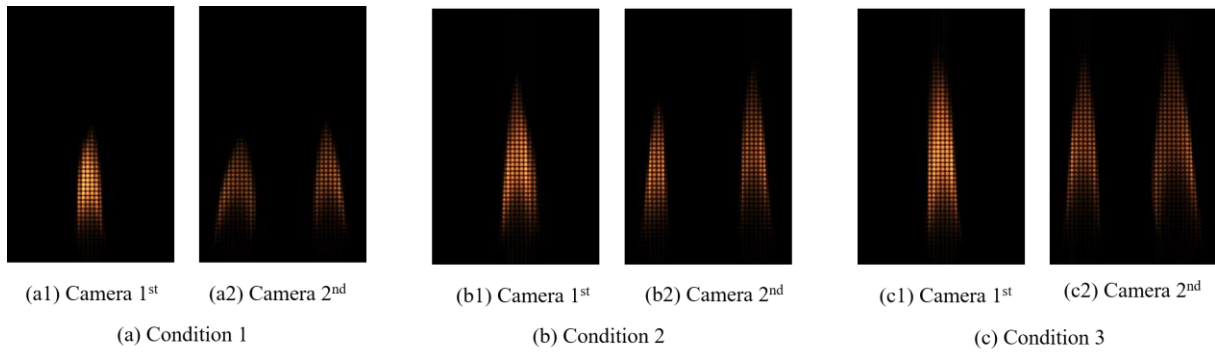


Fig. 14 Captured LF images under different conditions.

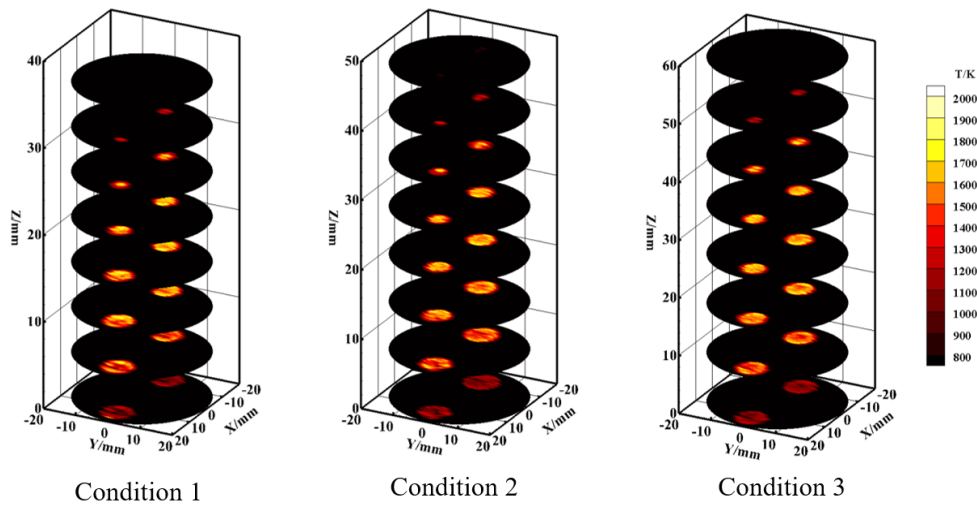


Fig. 15 The reconstructed bimodal flame temperature distributions over cross-sections under different operation conditions.

To compare the reconstructed temperature distributions by optimum and non-optimum angular arrangements, the LF flame images were also captured by non-optimum angular arrangements at 190° & 315° under condition 2. The LF flame images and reconstructed flame temperature distribution by non-optimum angular arrangement are shown in Fig. 16. Compare Fig. 16 (a) with Fig. 14 (b), the camera positioned at 277° can better reflect the relative position of the two modals, especially the distance between two modals. Further comparison of the reconstruction results can be seen that, although the profile of two flame modals can be reconstructed by the non-optimum angular arrangement, some regions were not successfully reconstructed, especially the flame modal at the left.

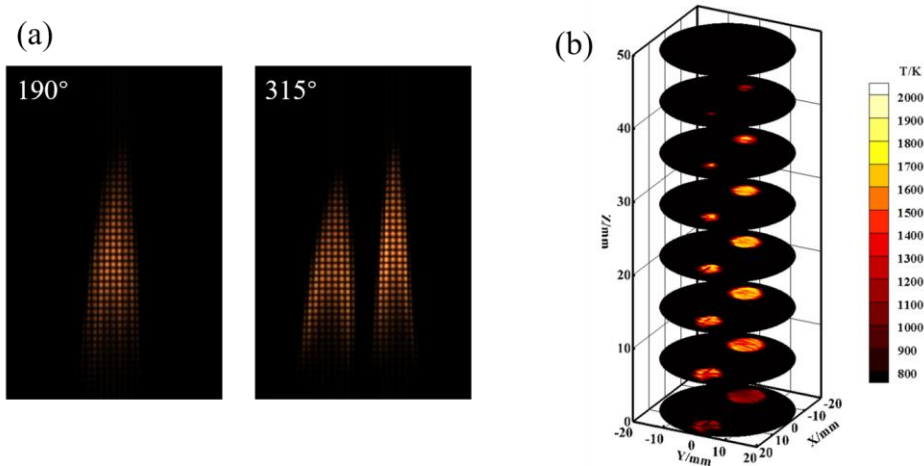


Fig. 16 The LF flame images and reconstructed temperature distribution by non-optimum angular arrangement.

To verify the reconstructed results, the R-type high precision thermocouple was also used to measure the flame temperature. Fig. 17 shows the experimental setup of flame temperature measurement using the thermocouple. The setup mainly comprises a motorized precision translation stage and a thermocouple. The translation stage can realize horizontal and vertical movement. The probe of the thermocouple is fixed on the translation platform to achieve temperature measurement at different positions. The flame temperature was measured at nine points along the flame diameter at $Z=15\text{mm}$. The flame temperature measured by the thermocouple was compensated systematically [46]. At each measurement point, 50 consecutive readings are taken. The standard deviations (STDs) for these readings are shown in Fig. 18. Fig. 18 also shows the reconstructed flame temperature compared to the thermocouple measurements. It can be noted that the reconstructed radial temperature is similar to the thermocouple measurements. The two measurements were observed to be in good agreement. The maximum difference between the reconstruction result and the thermocouple result is 83K and appears at $R=-15\text{mm}$, the cameras arranged at optimal angles can provide good reconstruction results.

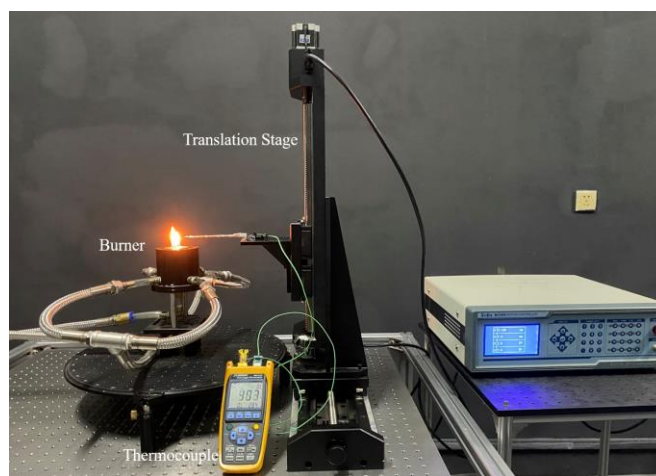


Fig. 17 Experimental setup of flame temperature measurement using a thermocouple

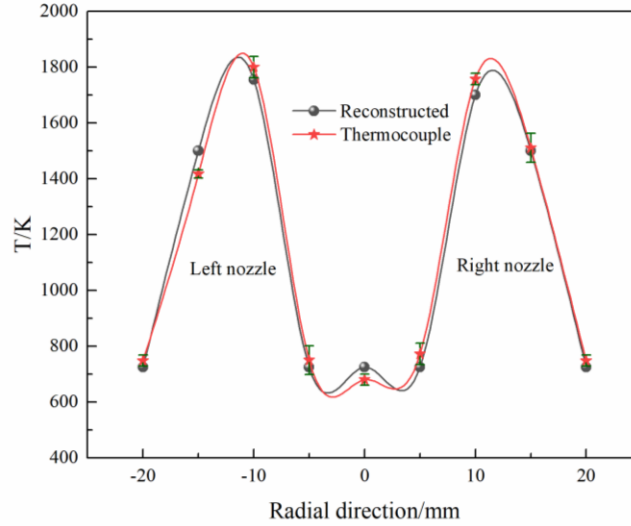


Fig. 18 The comparison of the reconstructed temperatures with the thermocouple measurement at $Z=15\text{mm}$ under Condition 1.

6. Conclusions

A novel angular arrangement optimization method of the multi-LF imaging technique is proposed to achieve optimal flame temperature reconstruction accuracy. Simulations systematically evaluate the proposed method under various angular arrangements, multi-LFC systems, and flame temperature distributions. Experiments were conducted on ethylene-air bimodal diffusion flames to reconstruct the temperature and thus verify the applicability of the method. The conclusions drawn from this study are summarized below.

- This study proposes an angular arrangement optimization method that uses the condition number of the reconstruction equation coefficient matrix as the objective function. The condition number is a good quantitative indicator of ill-conditioning of the reconstruction. The QPSO algorithm is an effective algorithm for optimising the angular arrangement of the multi-LF imaging technique.
- The condition number and reconstruction errors decrease with the increasing number of cameras, indicating the richer flame radiative information collected, the more accurate the flame temperature reconstructed.
- The proposed method enables optimization of the multi-LF imaging technique's angular arrangement under different flames.
- The proposed method can optimize the angular arrangement of the multi-LFC camera system, in which the number of cameras is not limited. This method can provide specific angular arrangement information for flames, not just angular separation.

Future work will focus on the application of the proposed method to the actual burner array of gas-turbine flames, as well as utilizing parallel techniques to improve the speed of the optimization process.

Acknowledgements

This work was supported by the National Natural Science Foundation of China [No. 51976038]; the fund of the State Key Laboratory of Technologies in Space Cryogenic Propellants [No. SKLTSCP1908]; and the Scientific Research Foundation of Graduate School of Southeast University [No. YBPY1951].

Reference

- [1] A.A. Subash, S. Yu, X. Liu, M. Bertsch, R.-Z. Szasz, Z. Li, X.-S. Bai, M. Aldén, D. Lörstad, Flame investigations of a laboratory-scale CECOST swirl burner at atmospheric pressure conditions, *Fuel*, 279 (2020) 118421.
- [2] H. Yang, Y. Wu, X. Zeng, X. Wang, D. Zhao, Partially-Premixed Combustion Characteristics and Thermal Performance of Micro Jet Array Burners with Different Nozzle Spacings, *J. Therm. Sci.*, 30 (2021) 1718-1730.
- [3] R. Menon, S.R. Gollahalli, Combustion Characteristics of Interacting Multiple Jets in Cross Flow, *Combust. Sci. Technol.*, 60 (1988) 375-389.
- [4] J. Choi, R. Rajasegar, T. Lee, J. Yoo, Development and characterization of swirl-stabilized diffusion mesoscale burner array, *Appl. Therm. Eng.*, 175 (2020) 115373.
- [5] J. Choi, W. Lee, R. Rajasegar, T. Lee, J. Yoo, Effects of hydrogen enhancement on mesoscale burner array flame stability under acoustic perturbations, *Int. J. Hydrogen Energy*, 46 (2021) 37098-37107.
- [6] M. Koyama, S. Tachibana, Technical applicability of low-swirl fuel nozzle for liquid-fueled industrial gas turbine combustor, *Fuel*, 107 (2013) 766-776.
- [7] W. Wu, A. Adeosun, R.L. Axelbaum, A new method of flame temperature measurement utilizing the acoustic emissions from laser-induced plasmas, *Proc. Combust. Inst.*, 37 (2019) 1409-1415.
- [8] N. Polydorides, A. Tsekenis, E. Fisher, A. Chighine, H. McCann, L. Dimiccoli, P. Wright, M. Lengden, T. Benoy, D. Wilson, G. Humphries, W. Johnstone, Constrained models for optical absorption tomography, *Appl. Opt.*, 57 (2018) B1-B9.
- [9] B. Lei, C. Zhao, B. He, B. Wu, A study on source identification of gas explosion in coal mines based on gas concentration, *Fuel*, 290 (2021) 120053.
- [10] S.S. Aphale, P.E. DesJardin, Development of a non-intrusive radiative heat flux measurement for upward flame spread using DSLR camera based two-color pyrometry, *Combust. Flame*, 210 (2019) 262-278.
- [11] C. Xu, W. Zhao, J. Hu, B. Zhang, S. Wang, Liquid lens-based optical sectioning tomography for three-dimensional flame temperature measurement, *Fuel*, 196 (2017) 550-563.
- [12] M.M. Hossain, G. Lu, D. Sun, Y. Yan, Three-dimensional reconstruction of flame temperature and emissivity distribution using optical tomographic and two-colour pyrometric techniques, *Meas. Sci. Technol.*, 24 (2013) 074010.
- [13] M.M. Hossain, G. Lu, Y. Yan, Optical Fiber Imaging Based Tomographic Reconstruction of Burner Flames, *IEEE Transactions on Instrumentation & Measurement*, 61 (2012) 1417-1425.
- [14] Q. Cheng, X. Zhang, Z. Wang, H. Zhou, S. Shao, Simultaneous Measurement of Three-Dimensional Temperature Distributions and Radiative Properties Based on Radiation Image Processing Technology

in a Gas-Fired Pilot Tubular Furnace, *Heat Transfer Eng.*, 35 (2014) 770-779.

[15] J. Floyd, A.M. Kempf, Computed Tomography of Chemiluminescence (CTC): High resolution and instantaneous 3-D measurements of a Matrix burner, *Proc. Combust. Inst.*, 33 (2011) 751-758.

[16] J. Sun, C. Xu, B. Zhang, M.M. Hossain, S. Wang, H. Qi, H. Tan, Three-dimensional temperature field measurement of flame using a single light field camera, *Opt. Express*, 24 (2016) 1118-1132.

[17] M. Levoy, Z. Zhang, I. Mcdowall, Recording and controlling the 4D light field in a microscope using microlens arrays, *J. Microsc.*, 235 (2010) 144-162.

[18] Todor Georgiev, A. Lumsdaine, Focused Plenoptic Camera and Rendering, *J. Electron. Imaging*, 19 (2010) 021106.

[19] Y. Liu, M.M. Hossain, J. Sun, B. Zhang, C. Xu, Investigation and optimization of sampling characteristics of light field camera for flame temperature measurement, *Chin. Phys. B*, 28 (2019) 034207.

[20] J.N. Klemkowsky, T.W. Fahringer, C.J. Clifford, B.F. Bathel, B.S. Thurow, Plenoptic background oriented schlieren imaging, *Meas. Sci. Technol.*, 28 (2017) 095404.

[21] D. Kelly, Development of a Multi-band Plenoptic Camera for High Temperature Measurements, Aerospace Engineering, Auburn University, Auburn, Alabama, 2020.

[22] H.M. Kim, Y.J. Yoo, J.M. Lee, Y.M. Song, A Wide Field-of-View Light-Field Camera with Adjustable Multiplicity for Practical Applications, *Sensors*, 22 (2022) 3455.

[23] H.M. Kim, M.S. Kim, S. Chang, J. Jeong, H.-G. Jeon, Y.M. Song, Vari-Focal Light Field Camera for Extended Depth of Field, *Micromachines*, 12 (2021) 1453.

[24] H. Liu, Q. Wang, W. Cai, Assessment of plenoptic imaging for reconstruction of 3D discrete and continuous luminous fields, *Journal of the Optical Society of America A*, 36 (2019) 149-158.

[25] B. Zhang, S. Wang, C. Xu, S. Wang, A fast inversion method for 2-D flame temperature measurement, *Instrumentation and Measurement Technology Conference*, 2017, pp. 1-6.

[26] Q. Qi, M.M. Hossain, B. Zhang, T. Ling, C. Xu, Flame temperature reconstruction through a multi-plenoptic camera technique, *Meas. Sci. Technol.*, 30 (2019) 124002.

[27] C.-Y. Niu, H. Qi, X. Huang, L.-M. Ruan, H.-P. Tan, Efficient and robust method for simultaneous reconstruction of the temperature distribution and radiative properties in absorbing, emitting, and scattering media, *J. Quant. Spectrosc. Radiat. Transfer*, 184 (2016) 44-57.

[28] R.R. La Foy, P. Vlachos, Multi-Camera Plenoptic Particle Image Velocimetry, 10th International Symposium on Particle Image Velocimetry, July 1-3, 2013, Delft, The Netherlands, 2013.

[29] T.W. Fahringer, B.S. Thurow, Plenoptic particle image velocimetry with multiple plenoptic cameras, *Meas. Sci. Technol.*, 29 (2018) 075202.

[30] D. Mei, J. Ding, S. Shi, T.H. New, J. Soria, High resolution volumetric dual-camera light-field PIV, *Exp. Fluids*, 60 (2019) 132.

[31] K. Korus, M. Salamak, M. Jasiński, Optimization of geometric parameters of arch bridges using visual programming FEM components and genetic algorithm, *Eng. Struct.*, 241 (2021) 112465.

- [32] S. Stephany, J.C. Becceneri, R.P. Souto, H.F. de Campos Velho, A.J. Silva Neto, A pre-regularization scheme for the reconstruction of a spatial dependent scattering albedo using a hybrid ant colony optimization implementation, *Appl. Math. Modell.*, 34 (2010) 561-572.
- [33] S.N. Omkar, R. Khandelwal, T.V.S. Ananth, G. Narayana Naik, S. Gopalakrishnan, Quantum behaved Particle Swarm Optimization (QPSO) for multi-objective design optimization of composite structures, *Expert Syst. Appl.*, 36 (2009) 11312-11322.
- [34] B. Zhang, H. Qi, S.-C. Sun, L.-M. Ruan, H.-P. Tan, Solving inverse problems of radiative heat transfer and phase change in semitransparent medium by using Improved Quantum Particle Swarm Optimization, *Int. J. Heat Mass Transfer*, 85 (2015) 300-310.
- [35] Y. Cai, J. Sun, J. Wang, Y. Ding, N. Tian, X. Liao, W. Xu, Optimizing the codon usage of synthetic gene with QPSO algorithm, *J. Theor. Biol.*, 254 (2008) 123-127.
- [36] X. Huang, H. Qi, X.-L. Zhang, Y.-T. Ren, L.-M. Ruan, H.-P. Tan, Application of Landweber Method for Three-Dimensional Temperature Field Reconstruction Based on the Light-Field Imaging Technique, *J. Heat Transfer*, 140 (2018) 082701.
- [37] J.D. Felske, C.L. Tien, Calculation of the Emissivity of Luminous Flames, *Combustion Science & Technology*, 7 (1973) 25-31.
- [38] D. Gu, Z. Sun, B.B. Dally, P.R. Medwell, Z.T. Alwahabi, G.J. Nathan, Simultaneous measurements of gas temperature, soot volume fraction and primary particle diameter in a sooting lifted turbulent ethylene/air non-premixed flame, *Combust. Flame*, 179 (2017) 33-50.
- [39] E. Süli, D.F. Mayers, *An introduction to numerical analysis*, Cambridge university press, 2003.
- [40] J. Sun, B. Feng, W. Xu, Particle swarm optimization with particles having quantum behavior, *Proceedings of the 2004 Congress on Evolutionary Computation (IEEE Cat. No.04TH8753)*, 2004, pp. 325-331 Vol.321.
- [41] L. Jing, X. Wenbo, S. Jun, Quantum-behaved particle swarm optimization with mutation operator, *17th IEEE International Conference on Tools with Artificial Intelligence (ICTAI'05)*, 2005, pp. 4 pp.-240.
- [42] Q. Qi, M.M. Hossain, J.-J. Li, B. Zhang, J. Li, C.-L. Xu, Approach to reduce light field sampling redundancy for flame temperature reconstruction, *Opt. Express*, 29 (2021) 13094-13114.
- [43] J. Sun, M.M. Hossain, C. Xu, B. Zhang, Investigation of flame radiation sampling and temperature measurement through light field camera, *Int. J. Heat Mass Transfer*, 121 (2018) 1281-1296.
- [44] C.L. Lawson, R.J. Hanson, *Solving Least Squares Problems*, Society for Industrial and Applied Mathematics, Philadelphia, 1995.
- [45] Y. Liu, M. Zhu, T. Wang, G. Lei, M.M. Hossain, B. Zhang, J. Li, C. Xu, Spatial resolution of light field sectioning pyrometry for flame temperature measurement, *Opt. Lasers Eng.*, 140 (2021) 106545.
- [46] C.S. McEnally, Ü.Ö. Köylü, L.D. Pfefferle, D.E. Rosner, Soot volume fraction and temperature measurements in laminar nonpremixed flames using thermocouples, *Combust. Flame*, 109 (1997) 701-720.

